Journal of Power Sources 194 (2009) 252–262

Contents lists available at ScienceDirect

Journal of Power Sources

journal homepage: www.elsevier.com/locate/jpowsour

Effect of substitution with Cr^{3+} and addition of Ni on the physical and electrochemical properties of $Ce_{0.9}Sr_{0.1}VO_3$ as a H_2S-active anode for solid oxide fuel cells

Nemanja Danilovic, Jing-Li Luo*, Karl T. Chuang, Alan R. Sanger

Department of Chemical and Materials Engineering, University of Alberta, Alberta, Canada T6G 2G6

ARTICLE INFO

Article history:
Received 19 March 2009
Received in revised form 22 April 2009
Accepted 23 April 2009
Available online 3 May 2009

Keywords:
Solid oxide fuel cell
Hydrogen sulfide
Methane
Anode catalyst
Perovskite

ABSTRACT

Whereas $Ce_{0.9}Sr_{0.1}Cr_{0.5}V_{0.5}O_3$ is an active fuel cell anode catalyst for conversion of only the H_2S content of 0.5% H_2S–CH_4 at 850 °C, inclusion of 5 wt% NiO to form a composite catalyst enabled concurrent electrochemical conversion of CH_4. A fuel cell with a 0.3 mm thick YSZ membrane and $Ce_{0.9}Sr_{0.1}Cr_{0.5}V_{0.5}O_3$ as anode catalyst had a maximum power density of 85 mW cm^{-2} in 0.5% H_2S–CH_4 at 850 °C, arising only from the electro-oxidation of H_2S. Using a same thick membrane, promotion of the anode with 5 wt% NiO increased the total anode electro-oxidation activity to afford maximum power density of 100 mW cm^{-2} in 0.5% H_2S–CH_4. The same membrane provided 30 mW cm^{-2} in pure CH_4, showing that the incremental improvement arose substantially from CH_4 conversion. Performance of each anode was stable for over 12 h at maximum power output. XPS and XRD analyses showed that an increase in conductivity of $Ce_{0.9}Sr_{0.1}Cr_{0.5}V_{0.5}O_3$ in H_2S-containing environments resulted from a change in composition and structure from the tetragonal oxide to monoclinic $Ce_{0.9}Sr_{0.1}Cr_{0.5}V_{0.5}(O,S)_3$.

1. Introduction

Solid oxide fuel cells (SOFCs) are high temperature electrochemical devices that electrochemically oxidize a fuel to produce electrical power with high potential efficiency [1]. A recognized advantage of SOFCs is fuel flexibility. SOFCs can be fuelled using a variety of fuels, including hydrogen, methane (both directly and with reformed methane), alcohols, and syngas (coal gas) [2–8]. The preferred anode material currently used for SOFCs consists of a cermet of Ni and YSZ. However, when using an impure H_2 fuel such as reformed methane, the cermet is poisoned by H_2S and catalyzes coking reactions, both of which are detrimental to operation of the SOFC [9–16]. Reforming methane, preventing carbon deposition from carbon containing fuels, and removing sulfur impurities from the fuel to below 5 ppm levels, each add to capital and operating costs of the SOFC stack. The additional plant required both adds to costs and increases the footprint of the SOFC powerplant, and so significantly limits the widespread application of SOFC technology. For these reasons, solid oxide fuel cells research is being directed to investigation and development of fuel cells capable of utilizing fuels containing impure H_2, CO and even sulfur-based fuels, instead of requiring very expensive pure H_2 [15–24]. To this end, there is interest in finding alternative anodes, including composite materials, that will catalyze methane oxidation but not carbon growth, and that are both active and stable in the presence of H_2S [15–24].

Recently we showed that $Ce_{0.9}Sr_{0.1}VO_3$ (CSV) is a potential anode catalyst for the direct oxidation of 0.5% H_2S-containing CH_4 [25], a model fuel for sulfur containing natural gas which is abundant in several locations including western Canada. In particular, the H_2S content is similar to that found in coal gas and reformed diesel fuels such as JP-8 [14]. However, we found that even though the material had exceptional conductivity and produced a significant power density of 140 mW cm^{-2} from the electrocatalytic oxidation of up to 5% H_2S–N_2, it was not active towards methane electro-oxidation. The CSV catalyst was fully active only on partial sulfidation, which resulted in a structure change from a tetragonal to a monoclinic perovskite structure with partial anion site occupation by both S^{2-} and O^{2-}.

Chromium oxide, Cr_2O_3, is a known hydrocarbon oxidation catalyst and it has a wide oxidation state stability range from $Po_2 = 1$ atm to $Po_2 = 10^{-20}$ atm [26,27]. We now will show that partial substitution of Cr for V in CSV to form $Ce_{0.9}Sr_{0.1}Cr_{0.5}V_{0.5}O_3$ (CSCV) improves redox stability of the catalyst, but by itself does not confer significant activity for methane conversion. Ni is also a well known CH_4 oxidation catalyst [28]. Hence we used a combination of CSCV and Ni for electro-oxidation of a feed having both H_2S and methane. In addition, we showed that a cermet comprising a combination of CSCV, Ni and YSZ had enhanced activity for methane electro-oxidation.

* Corresponding author. Tel.: +1 780 492 2232; fax: +1 780 492 2881.
E-mail address: Jingli.Luo@ualberta.ca (J.-L. Luo).

0378-7753/$ – see front matter © 2009 Elsevier B.V. All rights reserved.
doi:10.1016/j.jpowsour.2009.04.051

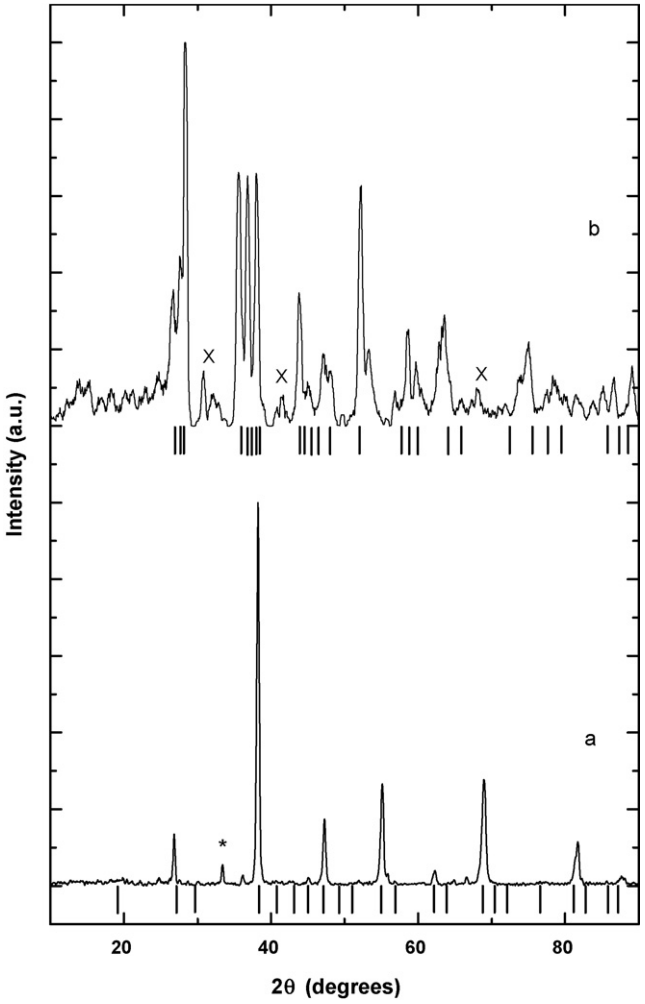

Fig. 1. XRD patterns of (a) $Ce_{0.9}Sr_{0.1}V_{0.5}Cr_{0.5}O_3$ (vertical lines indicate PDF# 25-0307) and (b) sulfided $Ce_{0.9}Sr_{0.1}V_{0.5}Cr_{0.5}O_3$ formed after conductivity test (vertical lines indicate PDF# 47-1039.) (*Indicates a small CeO_2 signal, × indicates an unknown phase.)

2. Experimental

2.1. Catalyst preparation

$Ce_{0.9}Sr_{0.1}VO_3$ (CSV) and $Ce_{0.9}Sr_{0.1}Cr_{0.5}V_{0.5}O_3$ (CSCV) were prepared by solid state synthesis from the powdered oxide precursors: SrO_2 (Alfa Aesar), CeO_2 (Sigma–Aldrich, 99.9%), V_2O_5 (Alfa Aeser, 98%) and Cr_2O_3 (Alfa Aesar, 99%). The powders were mixed in a ball mill for 24 h, sintered in alumina boats at 1100 °C in 1% H_2–Ar for 6 h. This procedure was repeated until the desired phase was formed as the single or predominant material, as shown by XRD analysis (Fig. 1). For CSCV fuel cell anodes, a nanopowder was prepared by the gel combustion synthesis method. Briefly, the procedure commenced by dissolving V_2O_5 in nitric acid, then admixing stoichiometric amounts of the nitrate salts $Ce(NO_3)\cdot 6H_2O$ (Acros Organics, 99.5%), $Sr(NO_3)_2$ (Alfa Aesar, 99%) and $Cr(NO_3)_3\cdot 9H_2O$ (Acros Organics, 99%). The mixture was stirred continuously on a hot plate at ~90 °C. Citric acid was added to form a 2:1 ratio of metal ions to acid. Ammonium hydroxide (Fisher Scientific) was added to balance the pH to ~7. The mixture was stirred further on the hot plate at 90 °C for several hours until the water had evaporated. The temperature was increased to 100 °C to form the sol–gel, followed by an increase to 300 °C to combust the gel. The porous foam formed after combustion was finely ground, then calcined in air at 900 °C for 2 h. The mixture subsequently was reduced in 1% H_2–Ar at 1100 °C for 2 h to form the required phase.

NiO was synthesized as a nanopowder by the same combustion synthesis method using $Ni(NO_3)_2\cdot 6H_2O$ (Alfa Aesar, 99.9985%), the gel from which was combusted and heated to 900 °C for 2 h.

NiO, CSCV and YSZ (Inframat Advanced Materials, 99.9%) were ball milled in a weight ratio of 5:47.5:47.5 for 24 h to form an intimately mixed composite anode cermet NiO–CSCV–YSZ (NCY).

2.2. Fuel cell testing

The anode catalyst (CSCV or NCY) powder was ground using a mortar and pestle, dispersed in α-terpineol to form a paste, and a 1 cm^2 area anode was screen printed onto a YSZ disk (8 mol% Y_2O_3, Intertec Southwest, 25.4 mm OD, 0.3 mm thick) electrolyte. The disk was pre-sintered in 1% H_2–Ar for 2 h at 1000 °C. Prior to testing, the cathode was prepared by painting platinum paste (Hereus, 1 cm^2) onto the cathode side of the button cell, and the membrane assembly (MEA) was fired in situ during the fuel cell test ramp-up. Typical anode thicknesses were ca. 50 μm, while the cathode thickness was 5–10 μm.

The MEA was installed in the fuel cell testing apparatus as shown and described in Ref. [25]. The anode and cathode chamber gas flow rates were each 100 mL min^{-1}, and the chamber volume was close to 80 cm^3, so the LHSV was about 75 h^{-1}.

Fuel cell tests were conducted using standard DC and AC electrochemical techniques with a two electrode set-up, a Solartron 1287A Potentiostat/Galvanostat (5 mV s^{-1} sweep rate was used for potentiodynamic tests) and a Solartron 1252A FRA (electrochemical impedance was analyzed from 1 MHz to 0.5 Hz, at OCV and ±20 mV). The wire resistance was manually compensated by externally measuring the wire resistance at testing temperature.

2.3. Conductivity testing

Conductivity measurements were conducted in a commercial NorECs Probostat electrochemical measurement cell using gold current collectors (two probes) in a single gas environment. Cylindrical pellets were prepared by pressing powdered catalyst at 2 tonnes in a 1 cm ID die, and the pellet so formed was fired at 1250 °C in 1% H_2–N_2 for 2 h. Gold paste was painted on both sides of the pellet and fired at 800 °C in 1% H_2–N_2 for 1 h. The combinations of gases used during the tests were 10% H_2–N_2 and 5% H_2S–N_2, each flowing at 50 mL min^{-1}. The samples were heated at 2 °C min^{-1} and tests were performed at selected temperatures in the range 500–950 °C. Measurements were made using the two-point DC conductivity method. The samples were held at testing temperature until a stable conductivity value was reached. Typically, in H_2 atmosphere stable values were obtained 2 h after stabilization of the testing temperature. Under a H_2S-containing environment the sample typically was held at 925 °C for 24 h before constant conductivity was achieved, whereas at lower temperatures stable conductivity values were achieved within 2 h.

2.4. Thermo-chemical characterization

Simultaneous differential scanning calorimetry–thermogravimetric analysis (DSC–TGA) was performed using a TA Instruments SDT Q600. The instrument has a horizontal balance which reduces buoyancy effects of the gas and prevents damage to the balance housing from reducing or corrosive gases.

For H_2S stability tests an accurately weighed ca. 20 mg powder sample was placed in an alumina cup (90 μL). The chamber was purged for 1 h. The sample was heated in a gas mixture comprising 100 mL min^{-1} N_2 and 1 mL min^{-1} of H_2 (1% H_2) at 20 °C min^{-1} to 850 °C at which temperature it was held for 30 min until the sig-

Table 1
Summary of BET surface areas of prepared catalysts.

	Material			
	CSV	CSCV		NCY
Preparation	Conventional	Conventional	Sol–gel	Sol–gel
BET (m^2/g)	1.2	1.1	5.9	38.1

nal stabilized. A feed comprising 500 ppm of H_2S (in N_2) flowing at 200 mL min^{-1} was then introduced to the chamber and maintained for 20–30 min. The sample was subsequently cooled in flowing N_2.

For oxidation–reduction measurements the samples, an accurately measured sample of about 10 mg of powder was placed in an alumina cup (90 μL), then the system was purged for 30 min using 100 mL min^{-1} flowing N_2 prior to testing. The samples were then heated to 1100 °C at 10 °C min^{-1} separately in each of the test gases: N_2, air and 1% H_2–N_2, flowing at 100 mL min^{-1}.

2.5. Materials characterization

A Rigaku RU200 powder X-ray diffraction (XRD) system with a rotating anode and a Co target was used for analysis of all synthesized powders, with a scan rate of $2^\circ\theta$ min^{-1}. The commercially available software Jade® was used for identifying phases present in the samples.

A Hitachi S-4800 field emission scanning electron microscope (SEM) was used for characterizing the cross-sections of MEAs.

X-ray photoelectron spectroscopy (XPS) was performed on the samples in a Kratos Analytical AXIS 165. A monochromated Al Kα ($h\nu$ = 1486.6 eV) source was used at a power of 210 W, with a base pressure of 3×10^{-8} Pa in the analytical chamber. Fixed analyser transmission (FAT) mode was applied with a resolution of 0.55 eV for Ag 3d and 0.70 eV for Au 4f peaks. The analysis spot was 700 μm × 300 μm. Charge neutralization (current 1.7 A, balance 1.8 V, bias 1.1 V) was applied to compensate for photoelectrons leaving the sample surface. After degassing, survey scans between 1100 and 0 eV were collected at a pass energy of 160, 0.35 eV step size and a dwell time of 200 ms, and data were merged over three scans. Narrow scans of Ce, V, Cr, O and S were collected at 20 eV pass energy, 0.1 eV step size and 200 ms dwell time and 10–20 scans per sample. Spectra were referenced to C 1s biding energy of 283.26 eV, and were fitted using Gaussian–Lorentzian peak shapes and Shirley baselines.

Quantachrome Instruments Autosorb I was used for BET surface area determinations of freshly prepared reduced catalysts.

3. Results

3.1. Characterization of anode materials

The XRD pattern of freshly prepared CSCV (PDF# 25-0307) showed the previously reported perovskite type structure for CSV, with a tetragonal unit cell and lattice parameters a = 5.52 Å and c = 7.81 Å (Fig. 1a) [25]. To form this structure Ce is present in the 3+ oxidation state, Cr as 3+, V as 3+ and Sr as 2+.

The BET surface areas of the prepared powders are summarized in Table 1. The high BET surface area of the NCY composite was due to the addition of nanoparticle YSZ. CSCV and the composite NCY each had good thermal expansion coefficient (TEC) matches with YSZ and so adhered well to the electrolyte. SEM images of prepared cross-sections of CSCV and NCY MEAs (Figs. 2 and 3) showed that both anodes adhered well to the YSZ electrolyte after sintering. CSCV catalyst particles were well dispersed, well interconnected, and the structure had good porosity. The NCY anode had well distributed phases YSZ, CSCV and Ni and a porous structure.

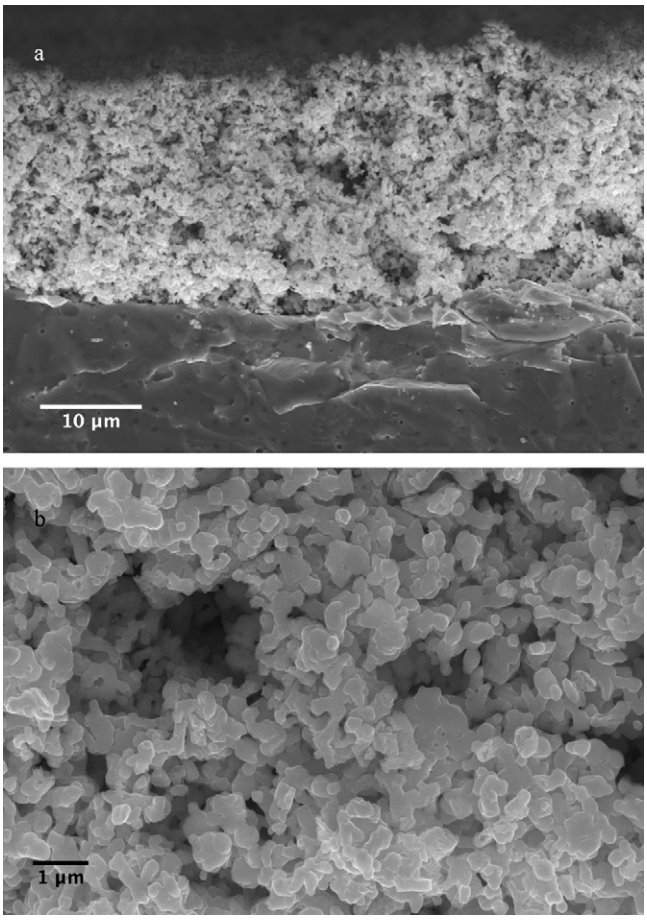

Fig. 2. SEM image of: (a) cross-section of CSCV MEA and (b) high magnification of $Ce_{0.9}Sr_{0.1}Cr_{0.5}V_{0.5}O_3$ anode.

3.2. Thermal analysis

The thermal stabilities of CSV and CSCV under oxidizing, inert and reducing environments were investigated using appropriate flowing gases in a DSC/TGA.

The TGA and DSC results for CSV are presented in Figs. 4 and 5, respectively. Fig. 4 shows a 7% total weight gain when the CSV oxidized from $Ce_{0.9}Sr_{0.1}VO_3$ to $Ce_{0.9}Sr_{0.1}VO_4$. $Ce_{0.9}Sr_{0.1}VO_4$ has a zircon-type tetragonal unit cell, with lattice parameters a = 7.36 Å and c = 6.49 Å (PDF# 12-0757) [25]. For this structure Ce must be in the 3+ oxidation state, V predominantly as 5+; again, and substituent Sr is 2+. The oxidation reaction occurred in two stages with an initial small weight increase that started about 300 °C, followed by a second major weight gain that started at 400 °C and was complete at 500 °C. The weight gain is due to incorporation of additional O, the first peak possibly attributable to oxidation of V^{3+} to V^{4+} and the second to oxidation to V^{5+}. During reduction there was a 6% weight loss, when $Ce_{0.9}Sr_{0.1}VO_4$ was reduced to $Ce_{0.9}Sr_{0.1}VO_3$, showing that the redox process was fully reversible. Reduction occurred much less readily than the oxidation reaction, as it started at 800 °C and finished at 950 °C. When $Ce_{0.9}Sr_{0.1}VO_3$ was heated under N_2 there was no weight change, and so there was no change in composition; however there was a phase change close to 400 °C. The DSC curves under reduction and oxidation conditions did not show any phase changes occurring independently of the oxidation and reduction reactions. Thus the reduction reac-

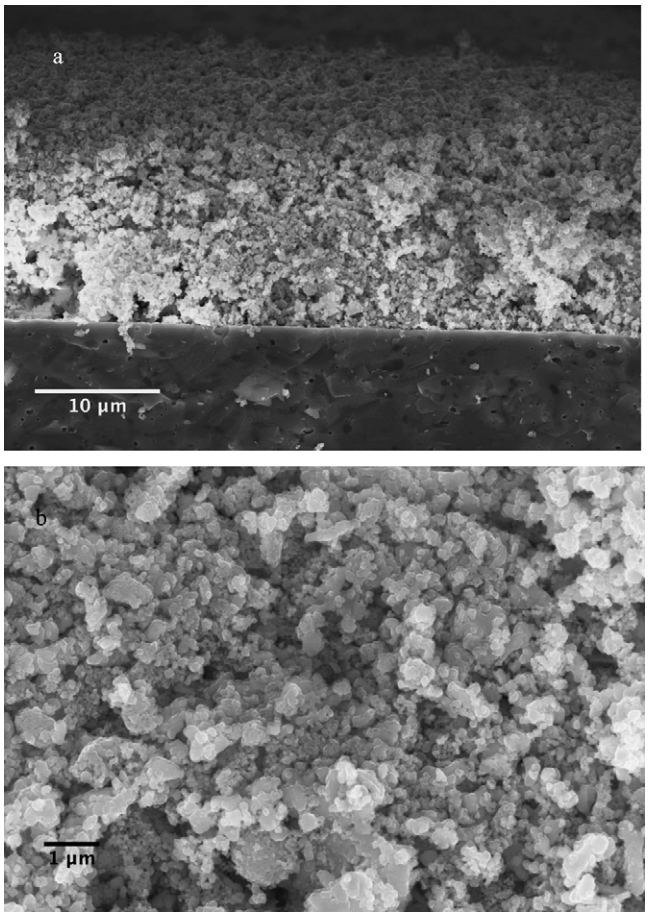

Fig. 3. SEM image of: (a) cross-section of NCY MEA and (b) high magnification of Ni–CSCV–YSZ anode.

tion may have been slower than oxidation as a consequence of the relative rates of the associated phase changes.

The TGA and DSC data for CSCV are presented in Figs. 6 and 7, respectively. CSCV gained 4% weight during oxidation, in a two-step process that started about 400 °C and was completed about 700 °C. The 4 wt% gain corresponds to an uptake of oxygen of only half ($Ce_{0.9}Sr_{0.1}Cr_{0.5}V_{0.5}O_{3.5}$) of what is required to fully oxidize

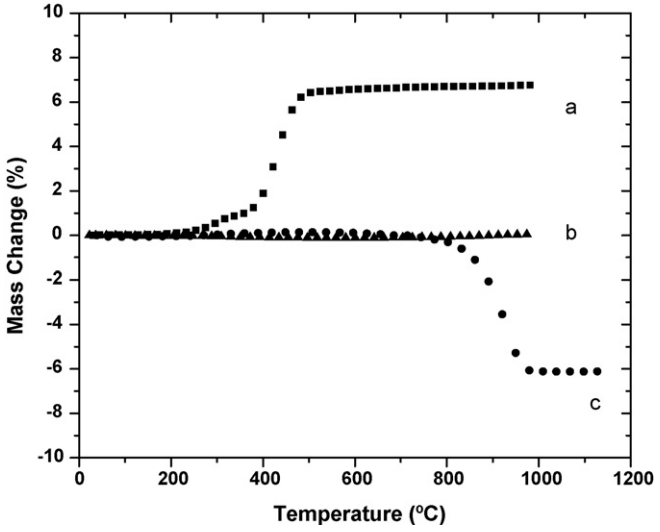

Fig. 4. TGA curves for (a) oxidation of $Ce_{0.9}Sr_{0.1}VO_3$ in air, (b) $Ce_{0.9}Sr_{0.1}VO_3$ in N_2 and (c) reduction of $Ce_{0.9}Sr_{0.1}VO_4$ in 1% H_2–N_2.

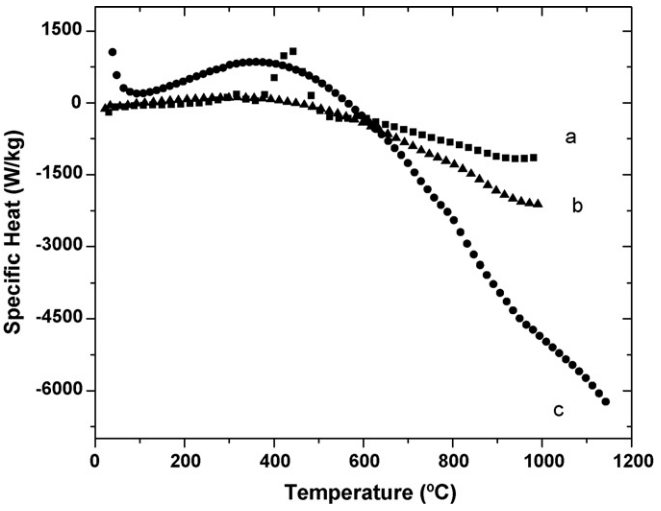

Fig. 5. DSC curves for (a) oxidation of $Ce_{0.9}Sr_{0.1}VO_3$ in air, (b) $Ce_{0.9}Sr_{0.1}VO_3$ in N_2 and (c) reduction of $Ce_{0.9}Sr_{0.1}VO_4$ in 1% H_2–N_2.

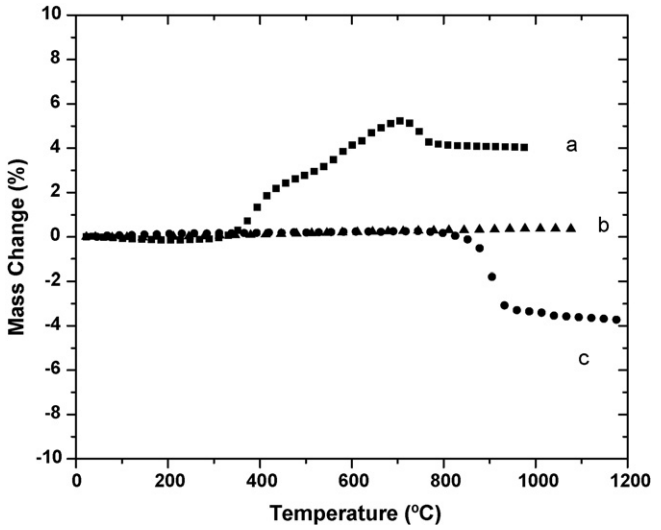

Fig. 6. TGA curves for (a) partial oxidation of $Ce_{0.9}Sr_{0.1}Cr_{0.5}V_{0.5}O_3$ in air, (b) $Ce_{0.9}Sr_{0.1}Cr_{0.5}V_{0.5}O_3$ in N_2 and (c) reduction of $Ce_{0.9}Sr_{0.1}Cr_{0.5}V_{0.5}O_{3+\delta}$ in 1% H_2–N_2.

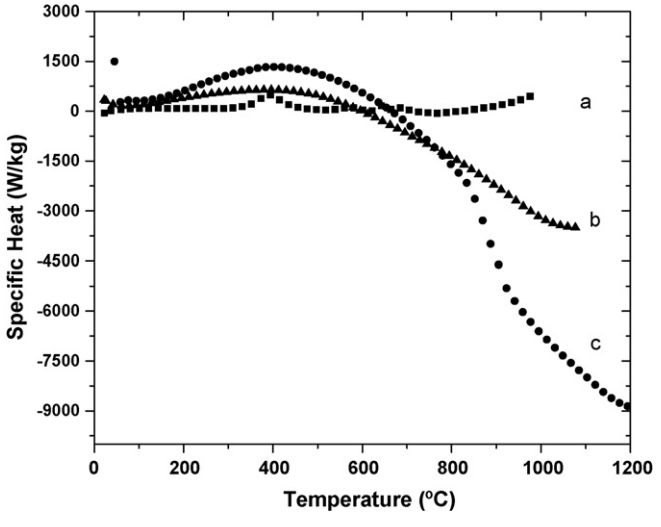

Fig. 7. DSC curves for (a) partial oxidation of $Ce_{0.9}Sr_{0.1}Cr_{0.5}V_{0.5}O_3$ in air, (b) $Ce_{0.9}Sr_{0.1}Cr_{0.5}V_{0.5}O_3$ in N_2 and (c) reduction of $Ce_{0.9}Sr_{0.1}Cr_{0.5}V_{0.5}O_{3+\delta}$ in 1% H_2–N_2.

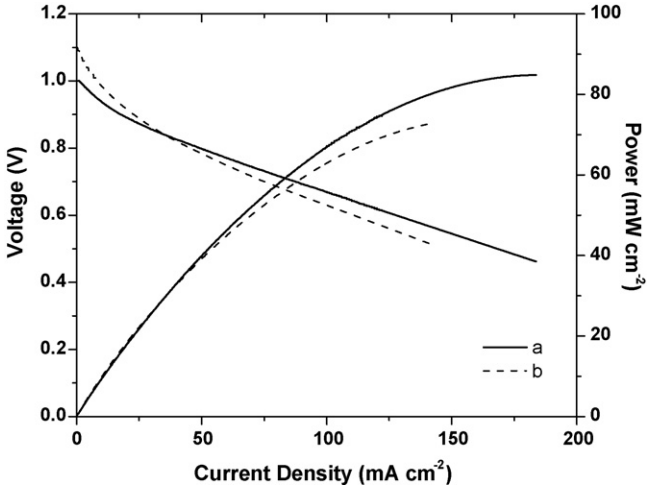

Fig. 8. Potentiodynamic curves for sulfided $Ce_{0.9}Sr_{0.1}Cr_{0.5}V_{0.5}O_3$|YSZ|Pt at 850 °C in: (a) 0.5% H_2S–N_2, and (b) 0.5% H_2S–CH_4.

the entire structure to $Ce_{0.9}Sr_{0.1}Cr_{0.5}V_{0.5}O_4$. Physically, this corresponds to oxidation of either half the V^{3+} to V^{5+} or all V^{3+} to V^{4+}, with a consequently greater oxygen coordination around the V cations. The process was reversible, as reduction of the oxidized CSCV also was 4 wt%, and occurred between 800 and 900 °C. No mass changes occurred under inert gas conditions, although there was a similar phase change at 400 °C, which was half as energetic as the one that occurred for CSV. Again, the DSC curves under reduction and oxidation conditions did not show any phase changes occurring independently of the oxidation and reduction reactions.

3.3. Electrochemical properties

Potentiodynamic tests were conducted to determine the electrochemical activity of the anode materials CSCV and NCY towards each of methane and H_2S. The MEAs were tested at 850 °C, in simulated sour gas comprising 0.5% H_2S–CH_4, 0.5% H_2S–N_2, 5% H_2S–N_2, and pure CH_4. Fig. 8 shows the IV and IP curves for CSCV|YSZ|Pt, in 0.5% H_2S–CH_4. With this feed the cell produced maximum power density 85 mW cm^{-2}, while in 0.5% H_2S–N_2 it was slightly lower, 75 mW cm^{-2}. In either pure CH_4 or H_2 the cell did not produce any measurable level of power.

In the methane containing fuel the open circuit voltage (OCV) was elevated to 1.1 V compared to about 1.0 V in N_2 containing H_2S, showing that CH_4 contributed to anode performance. Thus the difference in activity of the anode catalyst between feeds pure CH_4, 0.5% H_2S–CH_4 and 0.5% H_2S–N_2 did not arise from conversion of CH_4 over the unsulfided catalyst, but in the presence of H_2S the catalyst was partially sulfided, and this appeared to confer some capability to convert CH_4.

Fig. 9 shows impedance curves for CSCV under the conditions above, and performance data are compared in Table 2. The high frequency intercept, R_S, did not change significantly between the spectra when using different fuel feeds, and the value for R_{P1} (combined cathode and electrolyte resistance) was also similar in each

Table 2
Summary of impedance data.

	CSCV		Ni–CSCV–YSZ	
	0.5% H_2S–N_2 (Ω cm^2)	0.5%H_2S–CH_4 (Ω cm^2)	CH_4 (Ω cm^2)	0.5%H_2S–CH_4 (Ω cm^2)
R_S	1.7	1.7	2.3	1.4
R_{P1}	3.1	3.8	9.3	4.7
R_{P2}	1.2	3.3	2.0	1.2

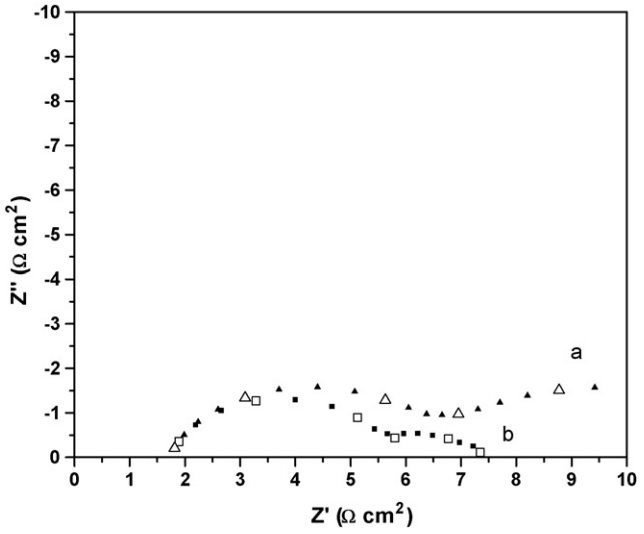

Fig. 9. Impedance spectra for sulfided $Ce_{0.9}Sr_{0.1}Cr_{0.5}V_{0.5}O_3$|YSZ|Pt at 850 °C in: (a) 0.5% H_2S–CH_4, and (b) 0.5% H_2S–N_2. (Frequency decades 1×10^5 to 1×10^{-1} are labelled with open symbols.)

case. In contrast, the value for R_{P2} (anode resistance) increased two-fold when using 0.5% H_2S–CH_4 and 0.5% H_2S–N_2.

For the MEA having the composite anode, NCY|YSZ|Pt MEA, the potentiodynamic curves obtained using CH_4 and 0.5% H_2S–CH_4 feed gases are shown in Fig. 10. The addition of Ni increased the activity of the anode for conversion of pure CH_4 and the maximum power density was 30 mW cm^{-2}. The power density using 0.5% H_2S–CH_4 as anode feed increased to 100 mW cm^{-2}. Impedance curves (Fig. 11) showed that the presence of H_2S in the gas improved the ohmic resistance, and also decreased the secondary polarization process. The high frequency intercept, R_S, was affected when the fuel was changed from pure methane to 0.5% H_2S–CH_4, as the CSCV portion of the composite anode was activated, thus reducing the resistance. The change in value for R_{P1}, the first electrode polarization resistance which is ascribed to the cathode in the CSCV case, represented an anode process in the composite NCY because the cathode resistance did not change as a result of the change in anode gas. Hence there was a shift in mechanism of the reaction from only a H_2S electrochemical reaction to inclusion of a CH_4 reaction. When pure CH_4 was used as the fuel R_{P1} was 9 Ω cm^2, and the value of R_{P1} decreased when CH_4 and H_2S competed for adsorption sites. The

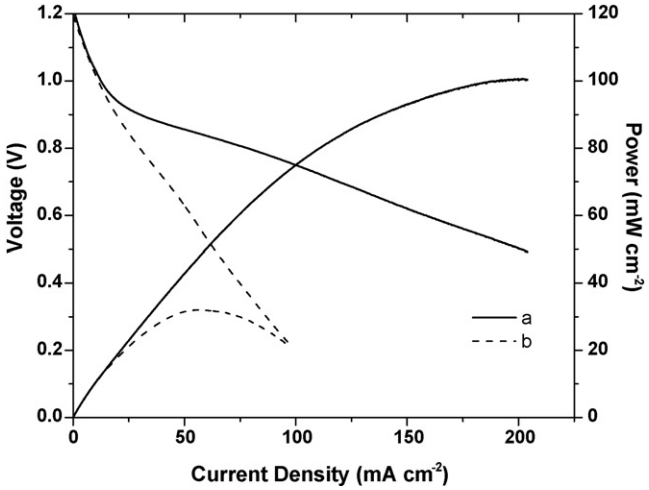

Fig. 10. Potentiodynamic curves for Ni–$Ce_{0.9}Sr_{0.1}Cr_{0.5}V_{0.5}O_3$–YSZ|YSZ|Pt at 850 °C in: (a) 0.5% H_2S–CH_4, and (b) CH_4.

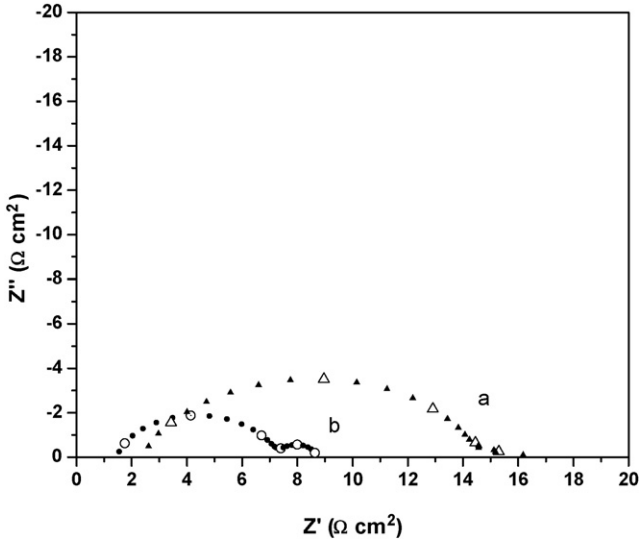

Fig. 11. Impedance spectra for Ni–$Ce_{0.9}Sr_{0.1}Cr_{0.5}V_{0.5}O_3$–YSZ|YSZ|Pt at 850 °C in: (a) CH_4, and (b) 0.5% H_2S–CH_4. (Frequency decades 1×10^5 to 1×10^{-1} are labelled with open symbols.)

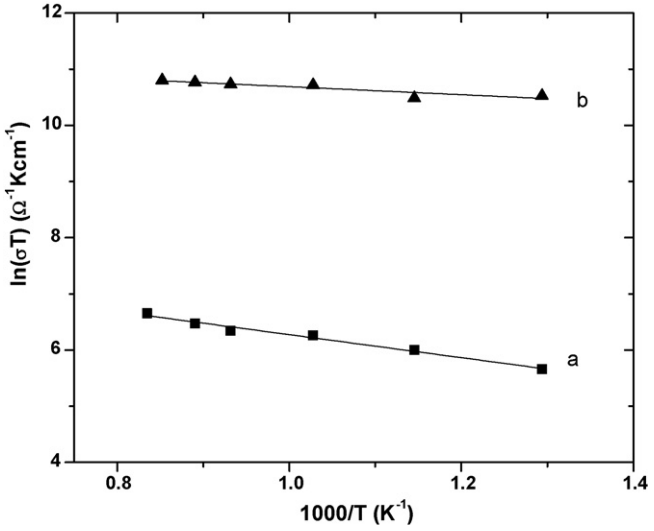

Fig. 13. Conductivity of $Ce_{0.9}Sr_{0.1}Cr_{0.5}V_{0.5}O_3$ in: (a) 10% H_2–N_2, and (b) sulfided catalyst in 5% H_2S–N_2.

second semicircle, representing the anode process, R_{P2}, decreased by about half when using 0.5% H_2S–CH_4 instead of pure CH_4, showing that the partially sulfided catalyst had lower resistance than the oxide form.

Fig. 12 compares the sustainability over 15 h of galvanostatic performance of the catalysts CSCV and NCY, with fuel cell output 75 and 40 mA cm^{-2}, respectively. The NCY anode was less stable than CSCV under galvanostatic conditions, as can be seen by the slight increase in overpotential from −0.65 to −0.6 V. This was most likely a consequence of one of two processes: sintering of the Ni particles, and poisoning of Ni sites by H_2S. Both processes are known to occur in SOFC systems containing Ni [9–16,29].

3.4. Total conductivity

The total conductivity of CSCV was determined under a range of conditions to determine the effects of atmosphere and temperature on its electrochemical properties. The conductivity of CSCV in H_2 increased with temperature, behaviour typical of semiconductors and ionic conductors (Fig. 13a). The activation energy was 0.1 eV. The conductivity of CSCV in H_2S-containing gas (Fig. 13b) increased slightly with increasing temperature, behaviour which indicated occurrence of two competitive processes arising from the combination of Cr and V. Without Cr addition, pure CSV showed conductivity behaviour typical of metallic conductors [25]. In H_2S the conductivity increased two orders of magnitude from 0.64 to 4.34 S cm^{-1} (at 900 °C), in contrast to behaviour in the H_2 environment, and the activation energy was much lower, −0.03 eV.

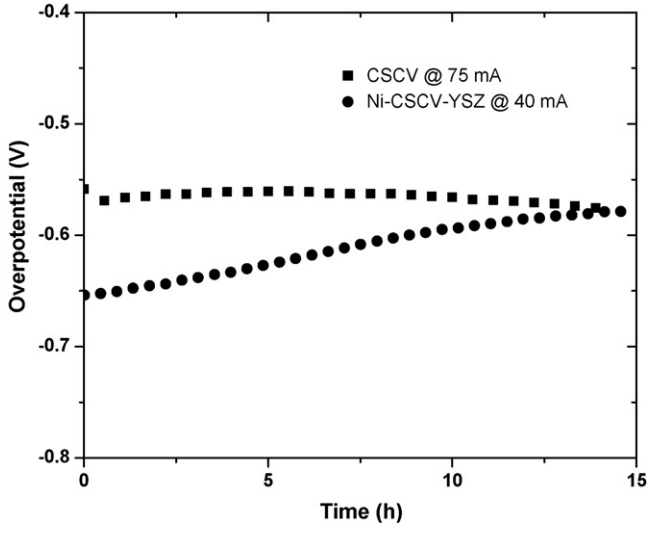

Fig. 12. Long-term galvanostatic test of sulfided $Ce_{0.9}Sr_{0.1}Cr_{0.5}V_{0.5}O_3$|YSZ|Pt and Ni–$Ce_{0.9}Sr_{0.1}Cr_{0.5}V_{0.5}O_3$–YSZ|YSZ|Pt at 850 °C.

XRD and XPS analyses were conducted on both fresh and used pellets to determine whether the change in conductivity was associated with changes in the composition and/or structure of the material, which were not evident visually. The gold electrode paste was removed, and the pellet was ground to a fine powder. XRD analysis of the powder showed that the material had undergone a chemical reaction with H_2S, to form a material having a structure similar to that of fully sulfided $Ce_{0.9}Sr_{0.1}V_{0.5}Cr_{0.5}S_3$. However, the XRD pattern is not fully consistent with that of $Ce_{0.9}Sr_{0.1}V_{0.5}Cr_{0.5}S_3$, as seen by comparing the peak positions and intensities with those of the fully sulfided compound (PDF# 47-1039) (Fig. 1b), and supported by the XPS results below. These findings are consistent with partial substitution of O by S in the oxide, which results in a phase change of the structure from tertragonal perovskite to monoclinic perovskite, resulting in the product $Ce_{0.9}Sr_{0.1}Cr_{0.5}V_{0.5}(O,S)_3$ [25].

3.5. H_2S stability

The CSCV and NCY anodes were also tested for H_2S reactivity at 850 °C. Both CSCV and NCY reacted with H_2S; the uptake of H_2S is shown in Figs. 14 and 15.

The weight and heat flow change were monitored before and during the reaction and TGA and DSC signals are shown in Fig. 14a and b, respectively. The signal was allowed to stabilize for ~30 min upon reaching the reaction temperature, during which reduction of the sample was still occurring. There was an initial increase in weight and an exothermic heat flow. The weight gain was 0.07475 mg which, assuming that it was totally ascribable to adsorbed H_2S, constituted 2.5×10^{18} molecules (4.15×10^{-6} mol). Assuming that chemisorbed H_2S dissociated to form a monolayer of adsorbed S atoms, and that the catalyst particle geometry was approximately spherical, this constituted about 14% partial surface coverage. The DSC signal also showed an exothermic peak followed

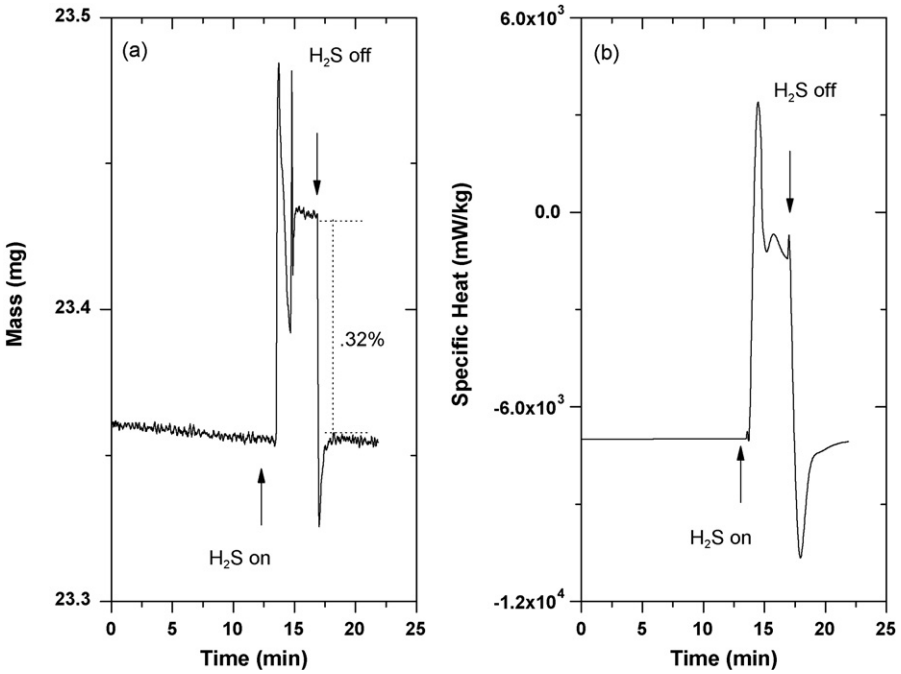

Fig. 14. Effect of 500 ppm of H_2S on: (a) TG, and (b) DSC signal of $Ce_{0.9}Sr_{0.1}Cr_{0.5}V_{0.5}O_3$ at 850 °C.

by an increased heat capacity, which was indicative of adsorption and a change in the phase of the material. After 15 min the H_2S flow was stopped and pure H_2 allowed to flow, which was followed, starting essentially immediately, by a gradual return to the original weight as the adsorbed S was desorbed as it reacted with H_2 to reform H_2S. Trace amounts of SO_2 were also detected in the effluent, attributed to continuing reaction of sulfur with oxygen anions to form SO_2. Since the DSC/TGA instrument used horizontal beams to position the samples in the reactive gas flow, buoyancy effects were minimized. Blank trials using empty alumina cups did not show the same response as those shown in Figs. 14 and 15, signifying that the reaction measured was dissociative adsorption of H_2S onto the catalyst sample.

The behaviour of the composite anode NCY differed from that of the component pure CSCV. In this case the material continuously adsorbed H_2S throughout the period of exposure, and when the supply of H_2S was terminated the adsorbed gas slowly desorbed from the material. During the 30 min of exposure to the gas, the weight of the material increased by 0.1047 mg or 5.82×10^{-6} mol H_2S.

3.6. XPS analyses

XPS was employed to determine the near-surface composition and near-surface ion electronic states of fresh CSCV, sulfided NCY, and sulfided $Ce_{0.9}Sr_{0.1}V_{0.5}Cr_{0.5}(O,S)_3$ which was formed after con-

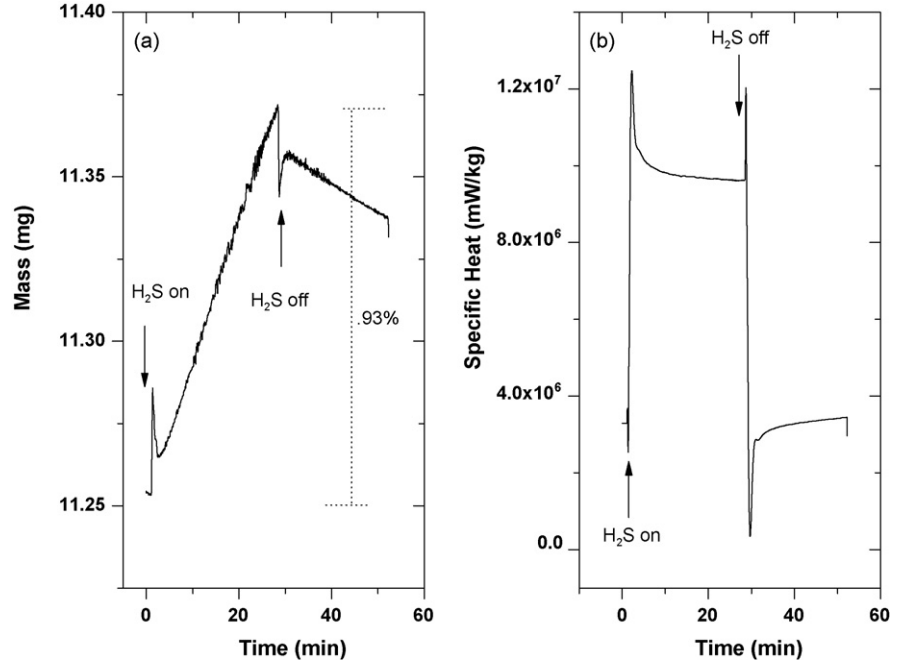

Fig. 15. Effect of 500 ppm of H_2S on: (a) TG, and (b) DSC signal of Ni–$Ce_{0.9}Sr_{0.1}Cr_{0.5}V_{0.5}O_3$–YSZ at 850 °C.

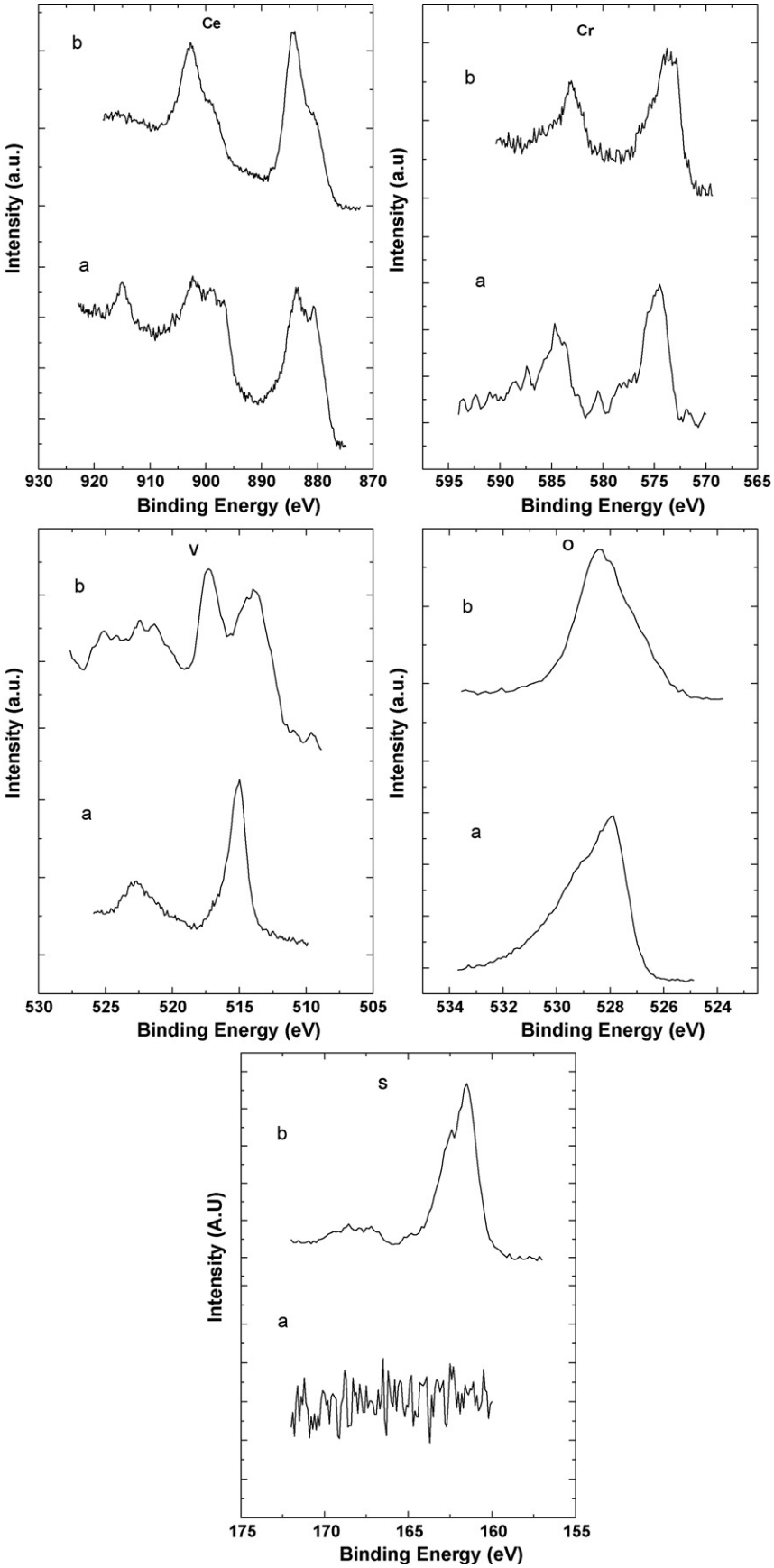

Fig. 16. XPS spectra for different elements of: (a) fresh, and (b) sulfided $Ce_{0.9}Sr_{0.1}Cr_{0.5}V_{0.5}O_3$.

Table 3
Summary of fitted XPS data.

	O		Ce				V			Cr			S			
	Ce-1s	V-1s	$3d^{5/2}$	$3d^{5/2}$	$3d^{3/2}$	$3d^{3/2}$	$3d^{3/2}$	$2p^{3/2}$	$2p^{1/2}$	$2p^{1/2}$	$2p^{3/2}$	$2p^{3/2}$	$2p^{1/2}$	$2p^{1/2}$	Sr-$2p^{3/2}$	V-$2p^{3/2}$	V-$2p^{1/2}$	Cc-$2p^{1/2}$
CSV																		
Area	2812.8	5493.4	3567.9	5164.2	3007.6	3678.9	1084.0	1565.1	348.0	340.1	342.2	105.2	146.8	260.7				
FWHM	1.2	2.8	3.3	4.2	3.8	5.2	2.7	1.5	2.8	1.8	2.2	3.2	2.0	7.0				
Position (eV)	527.9	529.2	880.1	883.7	897.2	901.5	914.8	515.1	521.4	522.8	574.6	577.2	584.2	587.2				
Concentration (%)	33.9	66.1	21.5	31.2	18.3	22.4	6.6	63.7	14.2	13.8	40.1	12.3	17.2	30.5				
CSV-S																		
Area	670.2	4116.7	4072.7	7092.8	2240.9	5630.2		630.5	300.4	243.7		495.9	547.9	405.6	115.9	667.9	1276.4	148.7	288.6
FWHM	1.5	2.1	3.7	3.4	3.5	4.2		2.9	1.5	3.7		1.8	3.0	2.2	2.4	1.1	2.7	0.9	2.9
Position	528.3	530.0	880.5	884.3	898.5	902.7		513.9	515.6	522.3		573.2	574.8	583.0	585.6	159.8	160.5	161.0	166.5
Concentration (%)	14.0	86.0	21.3	37.2	11.8	29.7		53.7	25.6	20.7		31.7	35.0	7.4	25.9	28.1	53.6	6.2	12.1

ductivity measurements in 5% H_2S-containing atmosphere. Fig. 16 shows high resolution sweeps of the main ionic components in the two materials. The compositions and peak locations are summarized in Table 3.

Ce had five peaks attributed to $d^{5/2}$ and $d^{3/2}$ orbitals in the fresh sample while there were only four peaks in the spectrum of the sulfided material. The highest energy peak for Ce, at 914.8 eV, was not present after sulfidation. The remaining four peaks all shifted to higher energies after sulfidation. The 880.5 and 883.8 eV peaks were shifted by about 0.5 eV, while the 897.2 and 901.5 eV peaks shifted by 1 eV to higher energies. The increase in binding energy may be related to an increase in oxidation state of a portion of Ce from Ce^{3+} to Ce^{4+} with sulfidation, since a more electropositive bond with S would decrease the binding energy. However, we will show below that the ratio of surface total anions/cations did not change by more than a small fraction, and so any partial change in oxidation state was small. It may therefore be that the change in peak position was attributable to a change in the anion bonded to the Ce cations.

The bond energy of the V peaks also had shifted following sulfidation. A new peak formed at 512.3 eV, which was at 3 eV lower than any V peak in the fresh CSCV sample. The $2p^{3/2}$ peaks at 515.1 and second peak 516.3 merged together to form one peak at 515.6 eV after sulfidation. A second peak was formed from the $2p^{1/2}$ peaks in the fresh sample at 521.4 and 522.9 eV merged into one peak at 520.7 eV after sulfidation. The decrease in binding energy of all of the peaks is consistent with V–S bonding replacing V–O bonding. The appearance of the 512.3 eV peak may have resulted from formation of a new, lower valence V species, possibly V^{2+}.

Bond energy shifts of the Cr peaks were similar to those of V after sulfidation. Three peaks from the fresh sample at 574.6, 584.2 and 587.2 eV each were shifted by about 1–1.5 eV to lower energies. One peak from the fresh sample at 577.2 was no longer present after sulfidation. The decrease in binding energy of all of the peaks signified formation of Cr–S bonding, similar to V.

Both O peaks shifted to higher binding energy by about 0.5 eV. The relative concentrations of the two peaks changed after sulfidation. Each binding energy representing a different bonding state for oxygen, as also occurred for sulfur as shown below, the first being a bridging O^{2-} between metal ions, the second being a terminal O^{2-} bonded to one metal ion.

There were four fitted peaks for sulfur on CSCV, which indicated bonding to each type of cation site. The spectrum for sulfur showed two pairs of overlapping peaks. The lower energy peak was attributed to a lattice sulfur, S^{2-}, while the higher energy peak was attributed to a bridging surface sulfur. These differed from the S adsorbed on NCY which showed only one peak centered at 167.2 eV (Fig. 17). It seemed that the surface predominantly consisted of primarily Ni and S, instead of a mixture of O and S in the case of pure CSCV.

Thus there was a change in the composition of the surface of the oxide which may have been, for example, from M–O–M(O)–O–M to either M–O–M(S)–O–M or M–S–M(O)–O–M, either of which would change the ratio of terminal surface O to bridging O, where M indicates a cation, –O– and –S– indicate bridging anions, and (O) and (S) indicate terminal O and S.

The oxygen to metal cation ratio (O/cat) at the surface of fresh CSCV was 2.45, whereas the sulfided CSCV had an O/cat ratio of 1.71 and a sulfur to cation ratio (S/cat) of 0.74. Thus the formulation of the sulfided materials is best represented by the formula $Ce_{0.9}Sr_{0.1}V_{0.5}Cr_{0.5}(S,O)_3$, for which the ratio of O/S was 2.33 and the surface (O+S)/cat ratio was 2.44. Hence the ratio of total surface anions/cations was the same in each case.

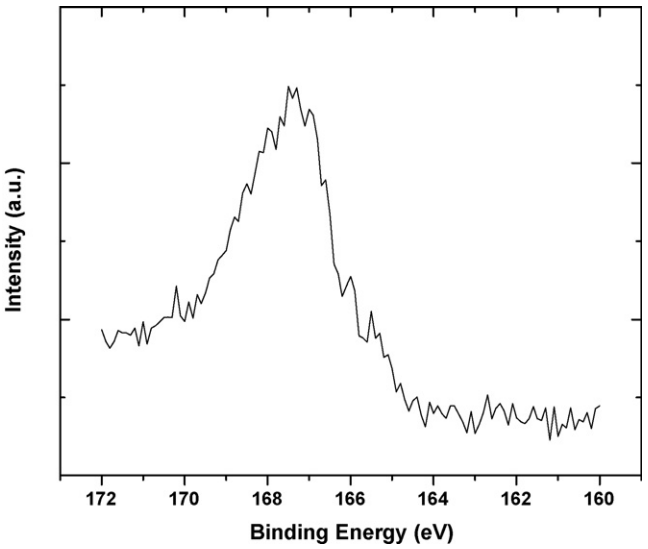

Fig. 17. XPS spectra for S region of Ni–$Ce_{0.9}Sr_{0.1}Cr_{0.5}V_{0.5}O_3$–YSZ after exposure to H_2S.

4. Discussion

The intimate combining of $CeVO_3$ with $CeCrO_3$ provided a substituted perovskite with better redox stability than the pure oxide $CeVO_3$, as shown by DSC/TGA. The perovskite parent lattice had the capability of accommodating both Cr and V cations at B-sites, due to their similar sizes. The Cr^{3+} ion is much more stable, as shown by Cr_2O_3 stability over a wide oxygen partial pressure range, and it appeared to stabilize the structure and stabilize V^{3+} at higher oxygen partial pressure conditions, as shown by the increased temperature required for oxidation and the lower weight increase during oxidation. The substitution of Cr at B-sites also almost doubled the total conductivity of the material compared to pure CSV in H_2 containing gas, from 0.33 to 0.57 S cm^{-1} at 850 °C [25]. Sr- or Ca-substituted $LaCrO_3$ is known to be a good electronic conductor, and it is used as a current collector material in SOFCs [30]. In the CSCV composite, the incorporation of Cr and the $Cr^{3+/4+}$ couple formed as a result of doping the structure with Sr imparts higher electronic conductivity compared to that of the V oxide, CSV.

In H_2S-containing gas the conductivity of CSCV drastically increased, from 0.57 to 42.27 S cm^{-1} at 850 °C. This drastic increase accompanied a phase change that occurred in the material, which XRD spectra showed to be formation of a partly sulfided phase of similar structure to tetragonal $Ce_{0.9}Sr_{0.1}V_{0.5}Cr_{0.5}S_3$. Texturing in the XRD spectra as well as the XPS results showing a O/S atomic ratio of 2.4 led to the conclusion that the material was an oxysulfide which had partial occupation of S^{2-} in O^{2-} sites in the tetragonal oxide perovskite. The ratio of total surface anions/cations was the same in each case, and so there was no oxidation. The change in structure accompanying partial sulfidation was similar to that found previously for $Ce_{0.9}Sr_{0.1}V(O,S)_3$ [25]. The continuing presence of O^{2-} in the structure enabled the fuel cell activity as the anode material must be electronically and ionically conductive, and no additional oxide ion conductor was added to the anode.

Potentiodynamic tests for CSCV showed that the anode was essentially inactive towards pure CH_4 and H_2. Upon heating the fuel cell to reaction temperature in H_2 environment the ohmic resistance of the cell was high, typically about 10 Ω cm^2 or greater. With the introduction of H_2S as a component of the fuel the resistance dropped and the altered catalyst, $Ce_{0.9}Sr_{0.1}V_{0.5}Cr_{0.5}(O,S)_3$, was highly active towards H_2S, although still not highly active to H_2 and CH_4. This is clearly seen in Fig. 8, where the fuel cell produced similar amounts of power with H_2S balanced with either CH_4 or N_2. If the anode catalyst was significantly active for conversion of CH_4, the activity would show a pronounced increase in performance in the presence of a high concentration of CH_4. This interpretation was supported by the impedance spectra shown in Fig. 9. The polarization resistance, as characterized by the second semicircle (the first semicircle is ascribed to the reaction at the Pt cathode), was higher in either N_2 or CH_4 alone. The anode was active for H_2S electro-oxidation in feeds containing either diluent, but the H_2S electro-oxidation reaction was impeded by either competitive adsorption (in the case of methane) or gas diffusion. The evidence for competitive adsorption of methane was that the OCV was higher when methane was used, consistent with have adsorption onto the surface under OCV conditions.

Substitution of transition metal cation Cr^{3+}, into the perovskite catalyst B-site of $Ce_{0.9}Sr_{0.1}VO_3$ resulted in an improvement in performance in 0.5% H_2S–N_2 in comparison to unsubstituted $Ce_{0.9}Sr_{0.1}VO_3$ [25]. The potentially active sites for H_2S oxidation were Ce, V and Cr cations. The mechanism was different from that for low temperature oxidation of H_2S over $CeVO_4$, where only $Ce^{3+/4+}$ was found to participate in the reaction [31], and similar to electrochemical activity of $Ce_{0.9}Sr_{0.1}VO_3$ were both Ce and V were found to participate in the H_2S electro-oxidation reaction over [25]. The evidence for participating cations in the reaction was found in the XPS data for sulfided CSCV: changes in bonding energies of the cations indicated their participation in the reaction mechanism. There was a peak associated with Ce^{4+} in the fresh oxide which disappeared after sulfidation, attributed to complete reduction of the Ce^{4+} cations during formation of the sulfided material. All the V and Cr peaks underwent shifts after sulfidation, and their binding energies were changed by at least 0.5 eV. In addition, two high energy peaks for both of Cr and V merged to form one peak.

The conductivity change resulting from the conversion of the oxide to sulfide was consistent with the high ohmic resistance of the material in non-H_2S-containing gases. The stability of CSCV towards carbon deposition and sulfur poisoning, as opposed to activation as a result of sulfidation, was confirmed by the long-term electrochemical tests in which performance did not degrade.

Ni and YSZ were added to CSCV to form a composite catalyst with the intent to improving methane oxidation kinetics of the anode. It was hypothesized that the presence of highly active oxide/sulfide around the Ni would prevent it from sulfiding in the sour gas, whereas, typically, 5 ppm of H_2S would poison Ni–YSZ anodes [9]. It was also recognized that the high H_2S concentration could enable favourable NiS formation [17–19]. The potentiodynamic and impedance data in Figs. 10 and 11 showed that the composite catalyst was active for methane conversion. Overall the composite produced 18% more power in sour gas, which was due to a combination of lower ohmic resistance and lower electrode polarization and gas diffusion impedance. A 15 h galvanostatic stability test at 40 mA cm^{-2} showed slight degradation of the potential from −0.66 to −0.6 V. This may have been a consequence of any one or combination of carbon deposition on the Ni particles, sulfur poisoning of the Ni, and agglomeration of Ni particles. Both DSC/TGA data and XPS data showed evidence of sulfidation of the anode. Under DSC/TGA conditions which simulated the atmosphere of the fuel cell, but without the potential gradient the anode adsorbed S continuously over 30 min. This differed from the uptake of H_2S on the CSCV anode alone for which the increase in weight ceased after adsorbing about 0.3% (w/w). The S XPS spectra for NCY differed from those for CSCV, in that there was evidence of primarily Ni–S bonds meaning that, even though H_2S-active CSCV sites were near the Ni sites, the H_2S still preferentially adsorbed onto Ni under fuel cell conditions.

5. Conclusions

- Cr^{3+} addition into CSV to form CSCV led to improved redox stability, and improved conductivity in reducing environments.
- CSCV had improved electrocatalytic activity towards H_2S oxidation compared to CSV; however Cr addition did not improve methane conversion activity. CSCV underwent a solid–gas reaction with H_2S in which the materials reacted to form $Ce_{0.9}Sr_{0.1}Cr_{0.5}V_{0.5}(O,S)_3$. The oxide retained in the MEA allowed continuing O^{2-} conduction.
- Admixing of NiO with CSCV increased methane oxidation activity, but the performance of Ni was not stable under the testing conditions.
- Ni–YSZ–CSCV and CSCV showed stable performance for 15 h under polarization conditions using H_2S–CH_4 as fuel.

Acknowledgments

This research was supported through funding to the NSERC Solid Oxide Fuel Cell Canada Strategic Research Network from the Natural Science and Engineering Research Council (NSERC). The authors would like to thank S. Merali (XRD), M. Danaie (SEM), D. Karpuzov and A. He (XPS), and B. Shalchi (BET) for assistance with characterization equipment.

References

[1] N.Q. Minh, Solid State Ionics 174 (2004) 271–277.
[2] F.Y. Wang, G.B. Jung, A. Su, S.H. Chan, X. Hao, Y.C. Chiang, J. Power Sources 185 (2008) 862–866.
[3] M.R. Pillai, I. Kim, D.M. Bierschenk, S.A. Barnett, J. Power Sources 185 (2008) 1086–1093.
[4] D.D. Burnette, G.G. Kremer, D.J. Bayless, J. Power Sources 182 (2008) 329–333.
[5] X.F. Ye, S.R. Wang, Z.R. Wang, L. Xiong, X.E. Sun, T.L. Wen, J. Power Sources 177 (2008) 419–425.
[6] H. Kishimoto, K. Yamaji, T. Horita, Y.P. Xiong, N. Sakai, M.E. Brito, H. Yokokawa, J. Power Sources 172 (2008) 67–71.
[7] Z.F. Zhou, R. Kumar, S.T. Thakur, L.R. Rudnick, H. Schobert, S.N. Lvov, J. Power Sources 171 (2007) 856–860.
[8] K. Xie, Q.L. Ma, B. Lin, Y.Z. Jiang, J.F. Gao, X.Q. Liu, G.Y. Meng, J. Power Sources 170 (2007) 271–277.
[9] J.N. Kuhn, N. Lakshminarayanan, U.S. Ozkan, J. Mol. Catal. A 282 (2008) 9–21.
[10] Z. Cheng, M. Liu, Solid State Ionics 178 (2007) 925–935.
[11] S. Zha, Z. Cheng, M. Liu, J. Electrochem. Soc. 154 (2007) B201–B206.
[12] H.P. He, A. Wood, D. Steedman, M. Tilleman, Solid State Ionics 179 (2008) 1478–1482.
[13] K. Haga, S. Adachi, Y. Shiratori, K. Itoh, K. Sasaki, Solid State Ionics 179 (2008) 1427–1431.
[14] M. Gong, X. Liu, J. Trembly, C. Johnson, J. Power Sources 168 (2007) 289–298.
[15] X.J. Chen, Q.L. Liu, S.H. Chan, N.P. Brandon, K.A. Khor, J. Electrochem. Soc. 154 (2007) B1206–B1211.
[16] Z.R. Xu, J.L. Luo, K.T. Chuang, A.R. Sanger, J. Phys. Chem. C 111 (2007) 16679–16685.
[17] C.M. Grgicak, R.G. Green, J.B. Giorgi, J. Power Sources 179 (2008) 317–328.
[18] C.M. Grgicak, J.B. Giorgi, J. Phys. Chem. C 111 (2007) 15446–15455.
[19] C.M. Grgicak, M.M. Pakulska, J.S. O'Brien, J.B. Giorgi, J. Power Sources 183 (2008) 26–33.
[20] X.C. Lu, J.H. Zhu, Solid State Ionics 178 (2007) 1467–1475.
[21] Y. Ji, Y.H. Huang, J.R. Ying, J.B. Goodenough, Electrochem. Commun. 9 (2007) 1881–1885.
[22] H. He, R.J. Gorte, J.M. Vohs, Electrochem. Solid-State Lett. 8 (2005) A279–A280.
[23] V. Vorontsov, J.L. Luo, A.R. Sanger, K.T. Chuang, J. Power Sources 183 (2008) 76–83.
[24] L. Aguilar, S. Zha, Z. Cheng, J. Winnick, M. Liu, J. Power Sources 135 (2004) 17–24.
[25] N. Danilovic, J.L. Luo, K.T. Chuang, A.R. Sanger, J. Power Sources, doi:10.1016/j.jpowsour.2009.03.045.
[26] T. Kawada, H. Yokokawa, in: J. Nowotny, C.C. Sorrell (Eds.), Key Engineering Materials, vols. 125–126, 1996, p. 205.
[27] I. Takahara, W.C. Chang, N. Mimura, M. Saito, Catal. Today 45 (1998) 55–59.
[28] J.B. Goodenough, Y.H. Huang, J. Power Sources 173 (2007) 1–10.
[29] S.P. Jiang, J. Mater. Sci. 38 (2003) 3775–3782.
[30] W.Z. Zhu, S.C. Deevi, Mater. Sci. Eng. A 362 (2003) 228–239.
[31] S. Yasyerli, G. Dogu, T. Dogu, Catal. Today 117 (2006) 271–278.